

Spectral variability of classical T Tauri stars accreting in an unstable regime

Ryuichi Kurosawa^{1,2*}, M. M. Romanova¹

¹*Department of Astronomy, Cornell University, Ithaca, NY 14853-6801, USA*

²*Max-Planck-Institut für Radioastronomie, Auf dem Hügel 69, 53121 Bonn, Germany*

4 November 2018

ABSTRACT

Classical T Tauri stars (CTTSs) are variable in different time-scales. One type of variability is possibly connected with the accretion of matter through the Rayleigh-Taylor instability that occurs at the interface between an accretion disc and a stellar magnetosphere. In this regime, matter accretes in several temporarily formed accretion streams or ‘tongues’ which appear in random locations, and produce stochastic photometric and line variability. We use the results of global three-dimensional magnetohydrodynamic simulations of matter flows in both stable and unstable accretion regimes to calculate time-dependent hydrogen line profiles and study their variability behaviours. In the stable regime, some hydrogen lines (e.g. $H\beta$, $H\gamma$, $H\delta$, $Pa\beta$ and $Br\gamma$) show a redshifted absorption component only during a fraction of a stellar rotation period, and its occurrence is periodic. However, in the unstable regime, the redshifted absorption component is present rather persistently during a whole stellar rotation cycle, and its strength varies non-periodically. In the stable regime, an ordered accretion funnel stream passes across the line of sight to an observer only once per stellar rotation period while in the unstable regime, several accreting streams/tongues, which are formed randomly, pass across the line of sight to an observer. The latter results in the quasi-stationarity appearance of the redshifted absorption despite the strongly unstable nature of the accretion. In the unstable regime, multiple hot spots form on the surface of the star, producing the stochastic light curve with several peaks per rotation period. This study suggests a CTTS that exhibits a stochastic light curve and a stochastic line variability, with a rather persistent redshifted absorption component, may be accreting in the unstable accretion regime.

Key words: line: profiles – radiative transfer – stars: variable: general – plasmas – magnetic fields – (magnetohydrodynamics) MHD

1 INTRODUCTION

Classical T Tauri stars (CTTSs) show variability in their light curves on time-scales from seconds up to decades (e.g. Herbst et al. 2002, Rucinski et al. 2008). The origin of variability is likely different for different time-scales. The long-term variability may be connected with the viscous evolution of the disc (e.g. Spruit & Taam 1993). The variability on the time-scales of a few stellar rotations may be connected with the inflation and closing of the field lines of the stellar magnetosphere (e.g. Aly & Kijpers 1990; Goodson, Winglee & Boehm 1997; Lovelace et al. 1995), which is supported by the observations of AA Tau (Bouvier et al. 2007). The variability on the time-scale of a stellar rotation are most likely connected with the rotation of a star, or with the obscuration of a stellar surface by a large-scale warped disc adjacent to the magne-

tosphere, which corotates with the star (e.g. Bouvier et al. 2003; Alencar et al. 2010; Romanova et al. 2013). The variability on even smaller time-scales may be connected with the accretion of individual turbulent cells formed in an accretion disc driven by magnetorotational instability (MRI) (e.g. Hawley 2000; Stone et al. 2000; Romanova et al. 2012). Another interesting possibility is that matter may accrete on to the star as a result of the magnetic Rayleigh-Taylor (RT) instability (e.g. Arons & Lea 1976; Spruit & Taam 1993; Li & Narayan 2004). Global three-dimensional (3D) magnetohydrodynamic (MHD) simulations (e.g. Romanova, Kulkarni & Lovelace 2008; Kulkarni & Romanova 2008, 2009) show that accretion proceeds through several unstable ‘tongues’, and the expected time-scale of the variability induced by the instability is a few times smaller than the rotation period of a star. The variability on the time-scale less than a second is also expected if the interaction of the funnel stream with the surface of the star leads to unstable radiative shocks which oscillate in a very short time-scale

* e-mail: kurosawa@mpifr-bonn.mpg.de

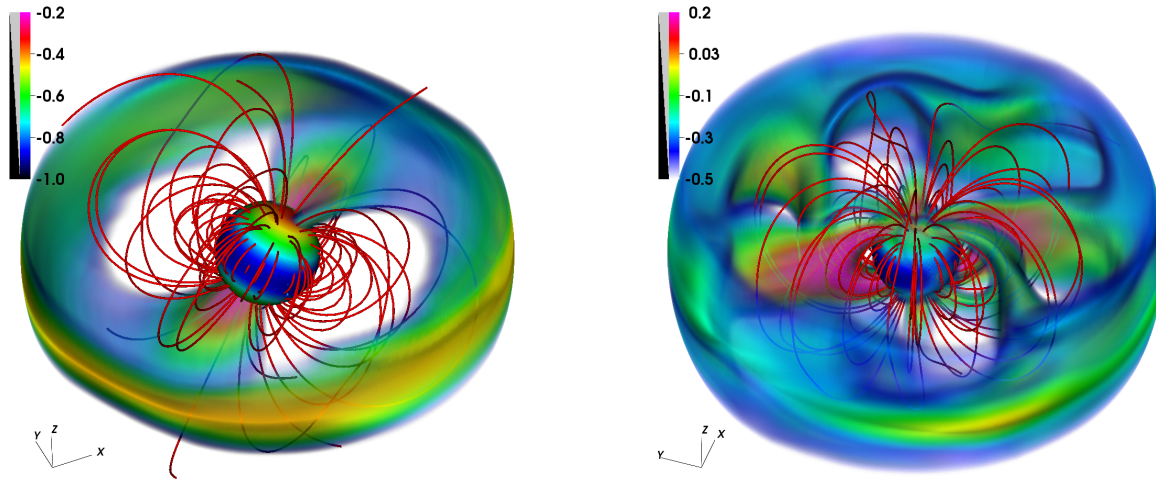


Figure 1. Examples of the magnetospheric accretions in a stable (left panel) and an unstable (right panel) regimes. The background colours show the volume rendering of the density (in logarithmic scales and in arbitrary units). The sample magnetic field lines are shown as red lines.

(e.g. Koldoba et al. 2008; Sacco et al. 2010). Finally, the variability can be also caused by magnetic flaring activities, which may occur on different time-scales (e.g. Herbst et al. 1994; Wolk et al. 2005; Feigelson et al. 2007).

Here, we concentrate on the variability associated with the unstable accretion caused by the RT instability, and study spectral properties of stars accreting in this regime. The global 3D numerical simulations performed earlier (e.g. Romanova et al. 2008; Kulkarni & Romanova 2008) show that randomly-forming tongues produce temporary hot spots on the stellar surface with irregular shapes and positions, and that the corresponding light curves are very irregular. Such irregular light-curves are frequently observed in CTTSs (e.g. Herbst et al. 1994; Rucinski et al. 2008; Alencar et al. 2010). However, the irregular light curve can be also produced, for example, by flaring activities. To distinguish the different mechanisms of forming irregular variability, we perform time-dependent modelling and analysis of emission line profiles of hydrogen.

To calculate the time-dependent line profiles from a CTTS accreting through the RT instability, we first calculate the matter flows in a global 3D MHD simulation with frequent writing of data. The fine time-slices of the MHD simulation data are then used as the input of the separate 3D radiative code TORUS (e.g. Harries 2000, 2011; Kurosawa et al. 2004; Kurosawa, Harries & Symington 2005, 2006; Symington, Harries & Kurosawa 2005; Kurosawa, Romanova & Harries 2011; Kurosawa & Romanova 2012). This allows us to follow the time evolution of the line profiles that occurs as a consequence of the dynamical nature of the accretion flows in the ‘unstable regime’. In earlier studies, we have used a similar procedure (of 3D+3D modelling) to calculate line spectra from a modelled star accreting in a ‘stable regime’ (using only a single time slice of MHD simulations) in which the gas accretes in two ordered funnel streams (Kurosawa et al. 2008). More recently, we have performed a similar modelling for a star with realistic stellar parameters (i.e. V2129 Oph), and have found a good agreement between the model and the time-series observed line profiles (Alencar et al. 2012). This example has shown that the combination of the 3D MHD and 3D radiative transfer (3D+3D) models is a useful

diagnostic tool for studying magnetospheric accretion processes. Examples of the magnetospheric accretion flows in both stable and unstable regimes are shown in Fig. 1.

In this paper, we use a similar 3D+3D modelling method as in the earlier studies, but will focus on the CTTSs accreting in the ‘unstable regime’. A model accretion in a stable regime is also presented as a comparison purpose. In the previous works, which focused on the stable regime, we have fixed the magnetospheric accretion at some moment of time (a single time slice of MHD simulations) to calculate line profiles; however, in the current work, we will use multiple moments of time from MHD simulations to investigate variability of hydrogen lines caused by the dynamical changes in the accretion flows. In particular, we focus on the variability phenomenon in the time-scale comparable with or less than a rotational period.

In Section 2, we describe numerical simulations of stable and unstable accretion flows along with our numerical methods used in the MHD and radiative transfer models. The model results are presented in Section 3. In Section 4, the model results are compared with observations. The discussion of the dependency of our models on various model parameters is presented in Section 5. Our conclusions are summarized in Section 6. Finally, some additional plots are given in Appendix A and in Appendix B in the online supporting information.

2 MODEL DESCRIPTION

To investigate variable line spectra from CTTSs in stable and unstable regimes of accretion, we perform numerical modelling in two steps. Firstly, we calculate the magnetospheric accretion flows using 3D MHD simulations and store the data at different stellar rotational phases. Secondly, we calculate hydrogen line profiles from the accretion flows, using the 3D radiative transfer code. For all the MHD and line profile models presented in this work, we adopt stellar parameters of a typical CTTS, i.e. its stellar radius $R_* = 2.0 R_\odot$ and its mass $M_* = 0.8 M_\odot$. Below, we briefly describe both models.

2.1 MHD models

We calculate matter flows around a rotating star with a dipole magnetic field with the magnetic axis tilted from the rotational axis by an angle Θ . The rotational axis of the star coincides with that of the accretion disc. A star is surrounded by a dense cold accretion disc and a hot low-density corona above and below the disc. Initially, a pressure balance is present between the disc and corona, and the gravitational, centrifugal and gas pressure forces are in balance in the whole simulation region (Romanova et al. 2002). The dipole field is strong enough to truncate the disc at a few stellar radii. To calculate matter flow, we solve a full set of magnetohydrodynamic equations (in 3D), using a Godunov-type numerical code (see Koldoba et al. 2002; Romanova et al. 2003, 2004, hereafter ROM04). The equations are written in the coordinate system that is corotating with the star. The magnetic field is split into the dipole component (B_d) which is fixed and the component induced by currents in the simulation region (B') which is calculated in the model. A viscosity term has been added to the code with a viscosity coefficient proportional to the α parameter (e.g. Shakura & Sunyaev 1973). The viscosity helps to form a quasi-stationary accretion in the disc. Our numerical code uses the ‘cubed sphere’ grid (Koldoba et al. 2002), and the Riemann solver used in the code is similar to that in Powell et al. (1999). This code has been used for modelling the magnetospheric flows in stable and unstable regimes of accretion in the past (Romanova et al. 2003; ROM04; Romanova et al. 2008; Kulkarni & Romanova 2008). It has been also used for modelling accretions to stars with a complex magnetic field (e.g. Long, Romanova & Lovelace 2007, 2008; Long et al. 2011; Romanova et al. 2011).

In this work, we study the simulations performed for the stable and unstable regimes of accretion (Fig. 1). Based on the previous numerical simulations of magnetospheric accretions on to neutron stars by Kulkarni & Romanova (2008) (see also Kulkarni & Romanova 2005), we select two sets of model parameters that are known to produce a stable and a strongly unstable regimes. However, we adjust some models parameters such that they become more suitable for a typical CTTs, and perform new MHD simulations. To keep a consistency, we adopt the same grid resolutions used in many of our earlier simulations (Romanova et al. 2008; Kulkarni & Romanova 2008, 2009), i.e. $N_r \times N^2 = 72 \times 31^2$ grid points in each of six blocks of the cubed sphere grid, which approximately corresponds to $N_r \times N_\theta \times N_\phi = 72 \times 62 \times 124$ grid points in the spherical coordinates.

The boundary conditions used here are similar to those in Romanova et al. (2003) and ROM04. At the stellar surface, ‘free’ [$\partial(\dots)/\partial r = 0$] boundary conditions to the density and pressure are applied. A star is treated as a perfect conductor so that the normal component of the magnetic field does not vary in time. A ‘free’ condition is applied to the azimuthal component of the poloidal current: $\partial(rB_\phi)/\partial r = 0$ such that the magnetic field lines have a ‘freedom’ to bend near the stellar surface. In the reference frame that is corotating with the star, the flow velocity is adjusted to be parallel to the magnetic field \mathbf{B} on the stellar surface ($r = R_*$), which corresponds to a frozen-in condition. The gas falls on to the surface of the star supersonically, and most of its kinetic energy is expected to be radiated away in the shock near the surface of the star (e.g. Camenzind 1990; Königl 1991; Calvet & Gullbring 1998). The evolution of the radiative shock above the surface of CTTs has been studied in detail by Koldoba et al. (2008). In this study, we assume all the kinetic energy of the flow is converted to thermal radiation (see ROM04 and Section 2.2) at the stellar sur-

	M_* (M_\odot)	R_* (R_\odot)	B_{eq} (G)	r_{cor} (R_*)	P_* (d)	Θ ($^\circ$)	α ($^-$)
Stable	0.8	2	10^3	5.1	4.3	30°	0.02
Unstable	0.8	2	10^3	8.6	9.2	5°	0.1

Table 1. Basic model parameters used for the stable and unstable regimes of accretions.

face. At the outer boundary ($r = R_{\text{max}}$), free boundary conditions are applied for all variables.

The key model parameters in our MHD simulations are: the stellar mass (M_*), stellar radius (R_*), surface magnetic field on the equator (B_{eq}), corotation radius (r_{cor}), stellar rotation period (P_*), tilt angle of dipole magnetic field with respect the disc axis (Θ) and α (viscosity) parameter. The parameter values adopted for the simulations in both stable and unstable regimes are summarized in Table 1. For more details on the simulation method and on the difference between the stable and unstable regimes, readers are referred to Romanova et al. (2003), ROM04, Romanova et al. (2008) and Kulkarni & Romanova (2008). Although we have adopted a relatively large viscosity coefficient $\alpha = 0.1$ for the model in the unstable regime (Table 1), to be consistent with our earlier models (Romanova et al. 2008; Kulkarni & Romanova 2008, 2009), our recent simulations have shown that the instability also develops with a smaller viscosity (e.g. $\alpha = 0.02\text{--}0.04$). More detailed discussion on the dependency of our model on different model parameters is presented in Section 5.

2.2 Radiative transfer models

For the calculations of hydrogen emission line profiles from the matter flow in the MHD simulations (Section 2.1), we use the radiative transfer code TORUS (e.g. Harries 2000, 2011; Kurosawa et al. 2006, 2011; Kurosawa & Romanova 2012). In particular, the numerical method used in the current work is essentially identical to that in Kurosawa et al. (2011); hence, for more comprehensive descriptions of our method, readers are referred to the earlier papers. In the following, we briefly summarize some important aspects of our line profile models.

The basic steps for computing the line variability are as follows: (1) mapping the MHD simulation data on to the radiative transfer grid, (2) source function (S_ν) calculations, and (3) observed line profile calculations as a function of rotational phase. In step (1), we use an adaptive mesh refinement (AMR) which allows for an accurate mapping of the original MHD simulation data onto the radiative transfer grid. The density and velocity values from the MHD simulations are mapped here, but the gas temperatures are assigned separately (see below). In step (2), we use a method similar to that of Klein & Castor (1978) (see also Rybicki & Hammer 1978; Hartmann, Hewett & Calvet 1994) in which the Sobolev approximation (e.g. Sobolev 1957; Castor 1970) is applied. The populations of the bound states of hydrogen are assumed to be in statistical equilibrium, and the continuum sources are the sum of radiations from the stellar photosphere and the hot spots formed by the funnel accretion streams merging on the stellar surface. For the photospheric contribution to the continuum flux, we adopt the effective temperature of photosphere $T_{\text{ph}} = 4000$ K and the surface gravity $\log g_* = 3.5$ (cgs), and use the model atmosphere of Kurucz (1979). The sizes and shapes of the hot spots are determined

by the local energy flux on the stellar surface (see Section 3.2 for more detail).

Our hydrogen model atom consists of 20 bound and a continuum states. In step (3), the line profiles are computed using the source function computed in step (2). The observed flux at each frequency point in line profiles are computed using the cylindrical coordinate system with its symmetry axis pointing toward an observer. The viewing angles of the system (the central star and the surrounding gas) are adjusted according to the rotational phase of the star and the inclination angle of the system for each time-slice of the MHD simulations. For both stable and unstable cases, the line profiles are computed at 25 different phases per stellar rotation. We follow the time evolution of the line profiles for about 3 stellar rotations; therefore, in total we compute 75 profiles for a given line transition.

The gas temperatures in the accretion funnels from the MHD simulations are in general too high ($T > 10^4$ K) when directly applied to the radiative transfer models, resulting in the lines being too strong. This is perhaps due to the 3D MHD simulations being performed for a pure adiabatic case (in which the equation for the entropy is solved). Solving the full energy equation would not solve the problem here because in both cases, the main issue is how the gas cools down at the inner disc and in the magnetospheric accretion flows. The process of cooling should involve cooling in a number of spectral lines, and is a separate complex problem. Hence, we use the adiabatic approach for solving 3D MHD equations in which we solve the equation for the entropy. To control the gas temperature in the radiative transfer calculations and to produce the line strengths comparable to those seen in observations, we adopt the parameterized temperature structure used by Hartmann et al. (1994) in which the gas temperatures are determined by assuming a volumetric heating rate proportional to r^{-3} , and by solving the energy balance of the radiative cooling rate (Hartmann, Avrett & Edwards 1982) and the heating rate. The same technique was also used by e.g. Muzerolle, Calvet & Hartmann (1998, 2001) and Lima et al. (2010). In our earlier work (e.g. Kurosawa et al. 2008), the high temperatures from MHD simulations were ‘re-scaled’ to lower values in order to match the line strengths seen in observations. However, we found that the line profiles computed with the re-scaled temperature were very similar to those computed with the parameterized temperature structure from Hartmann et al. (1994) (see Figure 7 in Kurosawa et al. 2008). Here, we adopt the latter as it is more physically motivated, but we expect to obtain similar line profiles even when we choose to use the re-scaled MHD simulation temperatures.

3 RESULTS

We perform two separate numerical MHD simulations for the magnetospheric accretion as described in Section 2.1 with the parameters shown in Table 1, which are known to produce a stable and an unstable magnetospheric accretion (e.g. Kulkarni & Romanova 2008). Typical configurations of matter flows in the stable and unstable regimes are shown in Fig. 1. While matter accretes in two ordered funnel streams in a stable regime, it accretes in several temporarily formed tongues, which appear in random locations at the inner edge of the accretion disc, in the unstable regime.

For the line and continuum variability calculations, we select the moments of time in the MHD simulations when the mass-accretion rates (\dot{M}) of the system become quasi-stationary over a few rotation periods. Note that \dot{M} for the unstable regime can

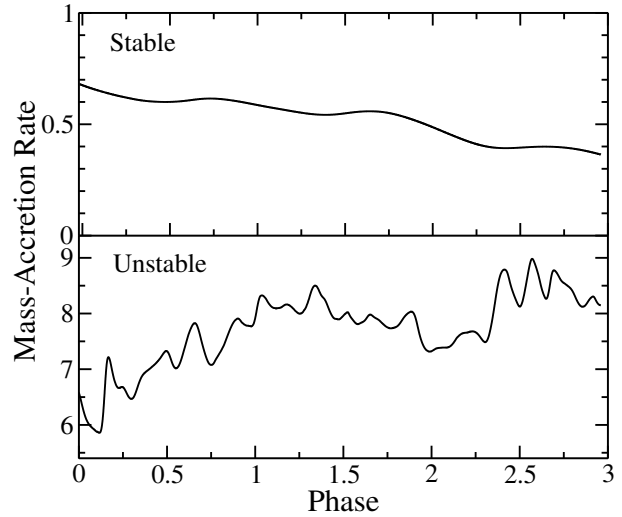


Figure 2. The mass accretion rates (in $10^{-8} M_{\odot} \text{ yr}^{-1}$) on to the central star plotted as a function of rotational phase for the stable (top) and unstable (bottom) cases.

be still variable in a shorter time scale. The MHD simulation outputs during 3 stellar rotation periods around these quasi-stationary phases are used in the variability calculations. The corresponding \dot{M} as a function rotational phase (ϕ) for the stable and unstable cases are shown in Fig. 2. According to the figure, for the stable case, \dot{M} rather steadily decreases by about 40 per cent during the 3 rotation periods. On the other hand, for the unstable case, \dot{M} increases slightly by about 20 per cent in 3 rotation periods, but it changes rather stochastically with smaller time-scales during those 3 rotation periods.

3.1 Line variability: persistent redshifted absorptions in the unstable regime

The output from the MHD simulations are saved with the rotational phase interval of $\Delta\phi = 0.04$, for 3 rotation periods. This corresponds to 75 total phase points at which line profiles are to be computed. This frequency is sufficient for ‘catching’ the main variability features in both stable and unstable regimes. For these moments of time, we calculate hydrogen lines profiles in optical and near-infrared i.e. $H\alpha$, $H\beta$, $H\gamma$, $H\delta$, $\text{Pa}\beta$ and $\text{Br}\gamma$ as a function of rotational phase, using the radiative transfer models as described in Section 2.2. We set the gas temperatures in the accretion funnels for both the stable and unstable cases to be between ~ 6000 K and ~ 7500 K. In all the variability calculations presented in this work, we adopt the intermediate inclination angle $i = 60^\circ$.

The subsets of the time-series line profile calculations for $H\alpha$, $H\beta$, $H\gamma$, $H\delta$, $\text{Pa}\beta$ and $\text{Br}\gamma$ are summarised in Figs. A1 and A2 (in Appendix A), with $\Delta\phi = 0.16$, for the first rotation period. A quick inspection of the figures shows that with these particular sets of model parameters (see above and Table 1), we find no clear redshifted absorption component caused by the accretion funnel flows in $H\alpha$ profiles, and only a weak redshifted absorption component is seen in $H\beta$ at some rotational phases. However, it is very notable in the higher Balmer lines ($H\gamma$ and $H\delta$), and also in the near-infrared lines ($\text{Pa}\beta$ and $\text{Br}\gamma$) partly because the peak fluxes in the emission part of the line profiles are relatively smaller than those of other lines ($H\alpha$ and $H\beta$). A similar tendency is also seen in some observations (e.g. Edwards 1979; Appenzeller, Jetter & Jankovics 1986;

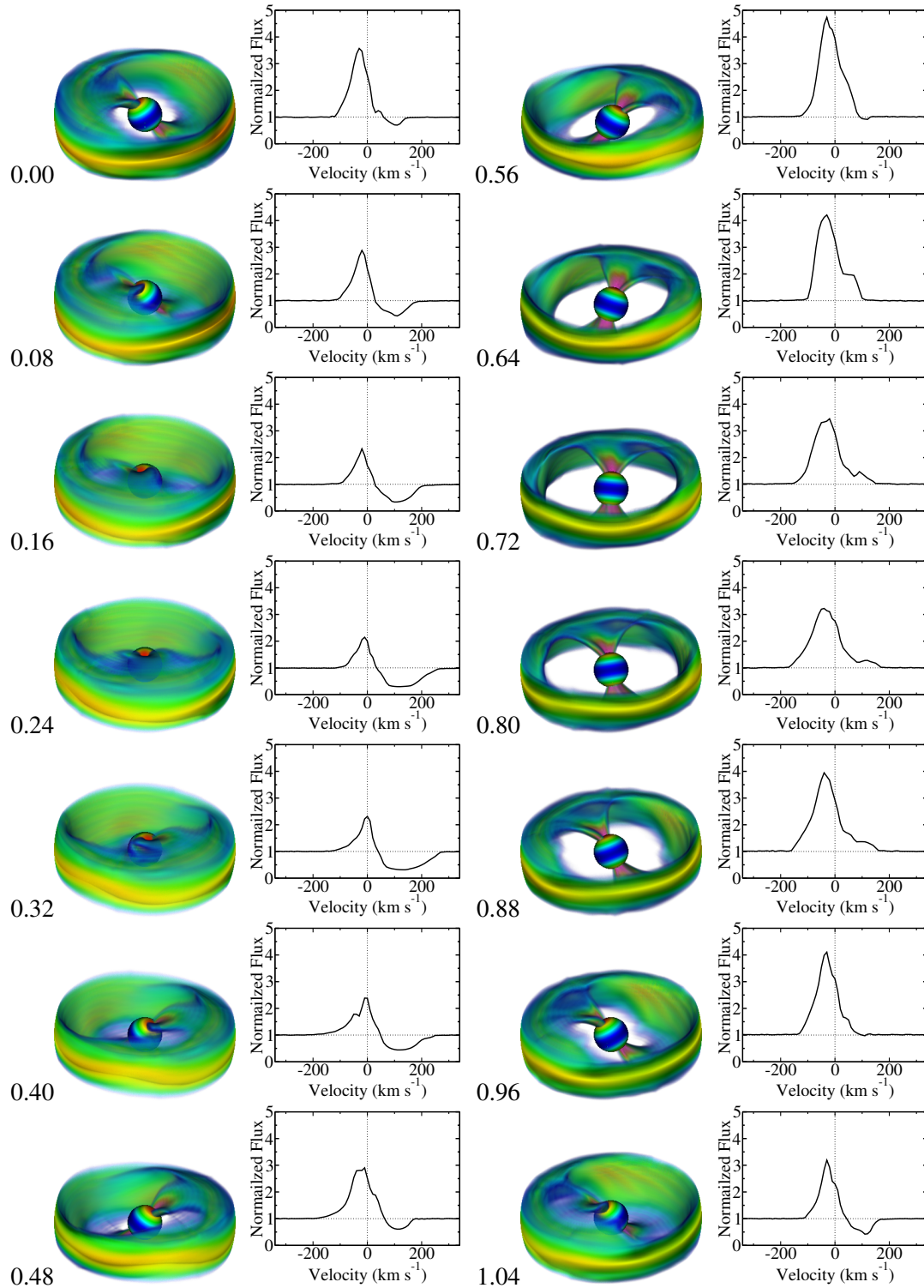


Figure 3. Magnetospheric accretion in the stable regime and the corresponding $H\delta$ model profiles are shown at different rotational phases (indicated at the lower-left corner of each panel; with 0.08 interval). For a demonstration purpose, only a subset (only for about one rotation period of the star) of the MHD simulations and model profiles is shown. The volume rendering of the density shown in colour (in logarithmic scale) at each phase are projected toward an observer viewing the system with its inclination angle $i = 60^\circ$. The model profiles are also computed at $i = 60^\circ$. Line profiles models extended to the rotational phase $\phi = 2.96$ are presented in Fig. B1 (Appendix B in the online supporting information).

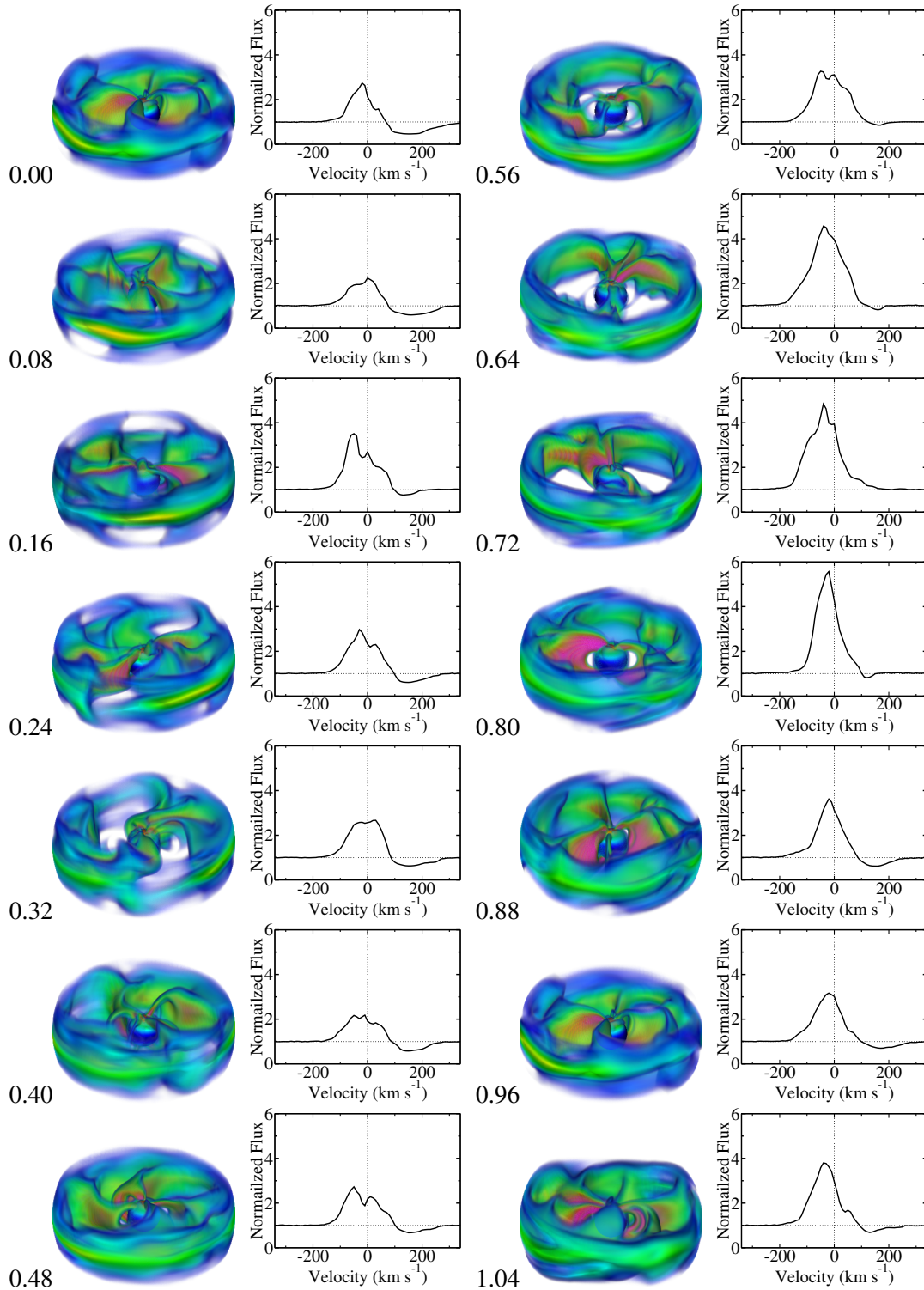


Figure 4. Same as in Fig. 3 but for the unstable regime. Line profiles models extended to the rotational phase $\phi = 2.96$ are presented in Fig. B2 (Appendix B in the online supporting information).

Krautter, Appenzeller & Jankovics 1990; Edwards et al. 1994). As a demonstration for differentiating the line variability seen in the stable and unstable cases, we mainly use the evolution of the redshifted absorption component in $H\delta$ profiles.

Fig. 3¹ shows the 3D views of the matter flows (the volume rendering of the 3D density distributions as seen by an observer

¹ The animated version of this figure, extended to three rotation periods, can be downloaded from http://www.astro.cornell.edu/~kurosawa/research/ctts_instab.html

with $i = 60^\circ$) as a function of rotational phases, for the star accreting in the stable regime. The change in the mass-accretion rate during the first rotation is fairly smooth according to Fig. 2, and the geometry of the accretion funnels is also very stable. The corresponding model line profiles of $H\delta$ are also shown in the same figure. It shows a subset of the time-series calculations, i.e. only the phases between $\phi = 0$ and $\phi = 1.04$ with the interval $\Delta\phi = 0.08$. The time-series of model $H\delta$ profiles during the whole 3 stellar rotations are given in Appendix B (Fig. B1) in the online supporting information. Fig. 3 shows that the redshifted absorption component starts appearing around $\phi \approx 0$, and its presence persists until $\phi \approx 0.5$. This phase span coincides with the time when the upper funnel accretion stream is located in front of the star, i.e., in the line of sight of the observer to the stellar surface. The redshifted absorption occurs when the hotspot continuum is absorbed due to the line opacity in the accretion flow which is, for the most part, cooler than the hotspots and moving away from the observer. Between $\phi \approx 0.5$ and 0.96, the redshifted absorption is not present because the lower accretion stream cannot intersect the line of sight of the observer to the hotspot. A similar behaviour was found in our earlier calculations with a stable accretion flow (Kurosawa et al. 2008). The appearance and disappearance of the redshifted absorption component is fairly periodic with their periods corresponding to the stellar rotation period (see also Fig. B1 in the online supporting information.).

A similar sequence of the 3D views of the matter flow in the unstable regime and the corresponding model line profiles for $H\delta$ are shown in Fig. 4². Again, the figure only shows a subset of the whole calculations, i.e. only for the phases between $\phi = 0$ and $\phi = 1.04$ with the interval $\Delta\phi = 0.08$. As before, the time-series of $H\delta$ profiles computed for 3 stellar rotations are given in the supplemental figure in Appendix B (Fig. B2) in the online supporting information. The figure clearly shows that the geometry of the accretion funnels and their evolution are very different from those of the stable case. The accretion no longer occurs in two streams, but rather occurs in the form of thin tongues of gas that penetrate the magnetosphere from the inner edge of the accretion disc (see also Romanova et al. 2008; Kulkarni & Romanova 2008). The shape and the number (up to a several) of the tongues change within one stellar rotation period. The corresponding mass-accretion rate, during these rotational phases, changes rather stochastically as seen in Fig. 2. According to Figs. 4 and B2 (Appendix B in the online supporting information), the peak strength of the line also changes stochastically. Interestingly, in the unstable regime, the redshifted absorption component is present at almost all rotational phases. This is caused by the fact that there are a few to several accretion streams/tongues in the system at all times, and at least one of the accretion stream is almost always in the line of sight of the observer to the stellar surface. This behaviour is clearly different from that in the stable regime in which the redshifted absorption appears and disappears periodically with a stellar rotation.

3.2 Photometric variability: stochastic variability in the unstable regime

In both stable and unstable regimes, matter accretes on to the star and forms hot spots on its surface. In our earlier work

(e.g. ROM04), the total kinetic energy of the gas accreting on to the stellar surface through the funnel streams are assumed to be radiated away isotropically as a blackbody. The effective temperature of a surface element in hot spots depends on the local energy flux at the surface element. The simulations show the hot spots are inhomogeneous with its highest energy flux and temperature in the innermost parts of spots. ROM04 have shown that the light curves in a stable regime are ordered/periodic, and have one or two maxima per period depending on the tilt angle of the dipole and on the inclination angle of the system. On the other hand, in an unstable regime, the light curves are usually stochastic because the equatorial accretion streams/tongues form stochastically and deposit the gas on to the stellar surface in a stochastic manner. This results in the stochastic formation of hot spots which produce the stochastic light curve (see also Romanova et al. 2008; Kulkarni & Romanova 2008). There is a wide range of possibilities when accretion is only weakly unstable in which both stable funnels and unstable tongues can coexist (Kulkarni & Romanova 2009; Bachetti et al. 2010). However, in this paper, we focus on the case of a strongly unstable regime as a demonstration.

As mentioned earlier, our MHD simulations lack an implementation of a proper cooling mechanism (e.g. radiative cooling), and consequently the adiabatically-heated gas in the funnel slows down gravitational acceleration of gas near the stellar surface. This results in the highest temperature of the hot spots to be only $T_{\text{hs}} \approx 4500\text{K}$ in the centre of the spot. This is not sufficient in explaining the ultraviolet radiation observed in many CTTs (e.g. Calvet & Gullbring 1998; Gullbring et al. 2000). Here, we use a slightly different approach for the light curve calculation from hot spots. To overcome the low hot spot temperatures, we simply set the temperature to $T_{\text{hs}} = 8000\text{K}$ regardless of the local energy flux at the hot spots. Consequently, the temperature is uniform over the hot spots. The shapes and the locations of the hot spots are determined by the energy fluxes computed at the inner boundary of the MHD simulation outputs. We apply a threshold energy-flux value such that the total hot spot coverage is about 2 per cent of the stellar surface (cf. Valenti, Basri & Johns 1993; Calvet & Gullbring 1998; Gullbring et al. 2000, Valenti & Johns-Krull 2004). The threshold energy-flux values are fixed for each sequence of the line profile computations (in the stable and unstable regimes separately) so that the hot spot sizes can evolve with time when the local energy flux on the stellar surface changes. The continuum radiation from the hot spots is included in the previous line variability calculation in Section 3.1. No separate continuum radiative transfer model have been performed, as the continuum flux calculations are performed as a part of line profile calculations. The resulting variability of the continuum flux (light curve) near $H\delta$ are shown in Fig 5 along with the hot spot distribution maps at four different rotational phases for both stable and unstable cases. The line wavelength of $H\delta$ is 4101 \AA which falls in a *B*-band filter; hence, the light curve shown here should be somewhat comparable to those from *B*-band photometric observations. The same figure also shows the corresponding line equivalent widths (EWs) for $H\delta$ as a function of rotational phase (cf. Figs. B1 and B2 in Appendix B in the online supporting information). Similar variability curves for other hydrogen lines, i.e. $H\alpha$, $H\beta$, $H\gamma$, $\text{Pa}\beta$ and $\text{Br}\gamma$ are summarized in Appendix A (Fig. A3).

The surface maps for the stable regime in Fig. 5 show the presence of banana-shaped hot spots on the stellar surface. For example, the hot spot on the upper hemisphere, which is created by the upper accretion stream (cf. Figs. 1 and 3), is visible on the surface maps at the rotational phases $\phi = 1.00$ and 1.24. The spot

² The animated version of this figure, extended to three rotation periods, can be downloaded from http://www.astro.cornell.edu/~kurosawa/research/ctts_instab.html

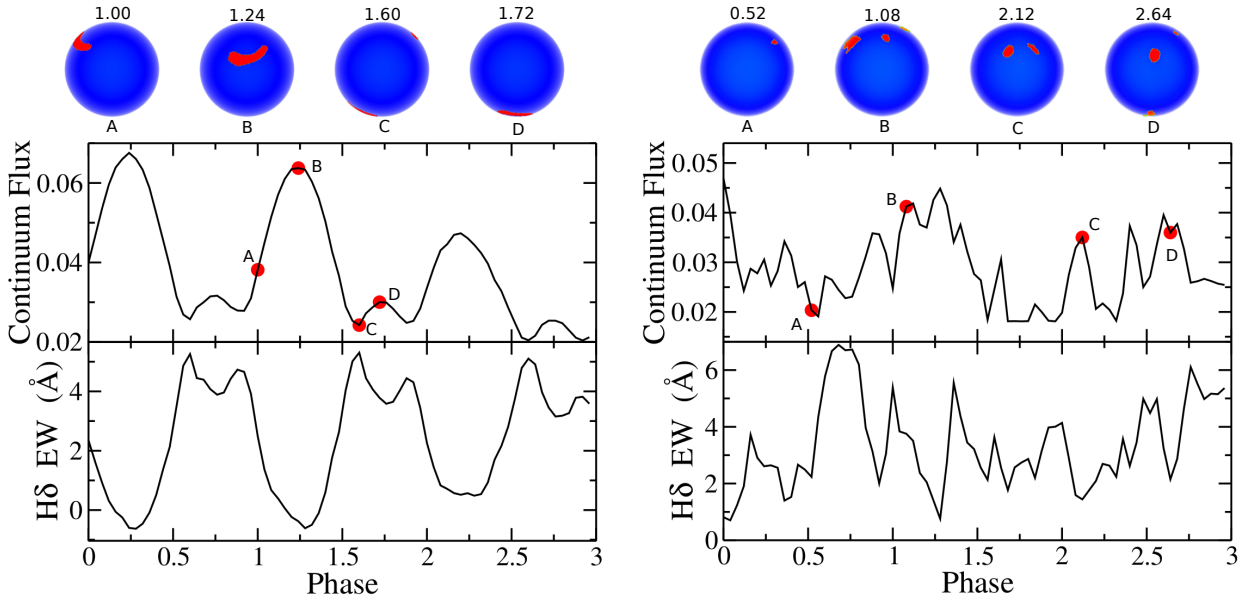


Figure 5. The maps of hot spots, as seen by an observer at the inclination angle $i = 60^\circ$, at four different rotational phases (top panels), the light-curves calculated at the wavelength of $H\delta$ (middle panels; flux in arbitrary units) and the line equivalent widths (EWs) of model $H\delta$ profiles (lower panels, in Å) are shown for the stable (left panels) and unstable (right panels) regimes of accretions. The hot spots are assumed to be radiating as a blackbody with $T = 8000$ K, and are shown for representative moments of time which are marked as red dots in the light curves.

on the lower hemisphere is visible, for example, at $\phi = 1.60$ and 1.72 . The light curve is periodic with its period corresponding to that of the stellar rotation. It is clearly seen that the maxima (at $\phi \approx 0.25, 1.25, 2.25$) of the light curve occur when the upper hot spot faces the direction of the observer. The smaller secondary peaks at $\phi \approx 0.75, 1.75, 2.75$ in the light curve are produced by the spot from the lower hemisphere. Interestingly, the line EW variability curves almost mirrors the light curve, i.e. it shows a similar variability pattern but the maxima of the light curve corresponds to the minima of the EW values³. This is caused by the combinations of the following: (1) for a given amount of line emission, the line EW decreases as the underlying continuum flux increases and (2) the amount of the redshifted absorption is largest when the accretion funnel on the upper hemisphere is directly in between the stellar surface and the observer. Geometrically, this corresponds to a phase when the upper hot spot points toward the observer. The shapes of the spots are fairly constant during the three rotation periods for which the light curves are evaluated. However, the peak of the light curves drop slightly in the later rotational phases since the mass-accretion rate decreases slightly during this time (see Fig. 2) and consequently the size of the spot decreases slightly.

In contrast to the smooth and periodic light curve seen in the stable case, the light curve (at the $H\delta$ wavelength) from the unstable case is highly irregular, and it resembles many of the observed light curves from CTTSs (e.g., Herbst et al. 1994, see also Section 4.2). The figure shows that there are typically several maxima per rotation period which correspond to several accretion tongues rotating around the star (Fig. 4). The stellar surface maps show that the number of hot spots visible to the observer changes in time. For example, only one spot is visible at $\phi = 0.52$, and multiple spots are visible at $\phi = 1.08$ (two spots), 2.12 (two spots), 2.54 (3 spots

– the third one is barely visible but present on the upper right edge). The sizes of individual spots also change in time as this should correlate with the mass-accretion rate seen in Fig. 2. The same figure also shows that the variability of $H\delta$ EW is also stochastic, and no clear periodicity is found. Unlike in the stable case, the line EW for the unstable case does not clearly mirror the light curves, but they tend to correlate with each other. This is likely caused by the fact the mass-accretion rate and the density in the funnel flows are not constant in time for the unstable case while they are almost constant in the stable case. An increase in the mass-accretion rate would cause an increase not only in the continuum flux but also in the line emission because the density in the funnel flows should also increase for the higher mass-accretion rate. This effect would make the light curve and the line EW tend to correlate each other, and the mirroring effect seen in the stable case becomes weakened or disappears. The light curves computed at other line frequencies (at $H\alpha$, $H\beta$, $H\gamma$, $Pa\beta$ and $Br\gamma$) have also shown similar qualitative behaviours, i.e. ordered curves in the stable regime of accretion, and stochastic curves in the unstable regime (see Fig. A3). In addition to the variable but rather persistent redshifted absorption component found in some lines (Figs. 4, A2 and B2 – Appendix B in the online supporting information), the stochastic light curves and stochastic EW variability (Figs. 5 and A3) are also key signatures of the CTTSs accreting in the unstable regime.

4 COMPARISONS WITH OBSERVATIONS

4.1 Line Variability

Many spectral line variability observations of CTTSs, in different time-scales, have been carried out in the past (e.g. Aiad et al. 1984; Edwards et al. 1994; Johns & Basri 1995a,b; Gullbring et al. 1996; Petrov et al. 1996; Chelli et al. 1997; Smith et al. 1999; Petrov et al. 1999; Oliveira et al. 2000; Petrov et al. 2001; Alencar & Batalha

³ In this paper, the sign of line equivalent widths (EWs) is opposite of that in a usual definition, i.e. a EW value is positive when the line is in emission.

2002; Stempels & Piskunov 2002; Alencar et al. 2005; Kurosawa et al. 2005; Bouvier et al. 2007; Donati et al. 2007; Donati et al. 2008, 2010, 2011a,b; Alencar et al. 2012; Costigan et al. 2012; Faesi et al. 2012). The line variability is often used to probe the geometry of magnetospheric accretion flows, and in many cases the accretion flows are found to be non-axisymmetric, e.g. SU Aur (e.g. Johns & Basri 1995b; Petrov et al. 1996) and RW Aur A (e.g. Petrov et al. 2001). One of the key signatures of magnetospheric accretion is the presence of the redshifted absorption component in line profiles. Such absorption components have been observed e.g. in some Balmer lines (e.g. Aiad et al. 1984; Appenzeller, Reitermann & Stahl 1988; Reipurth et al. 1996), in near-infrared hydrogen lines ($\text{Pa}\beta$ and $\text{Br}\gamma$, e.g. Folha & Emerson 2001) and in some helium lines (e.g. Beristain, Edwards & Kwan 2001; Edwards et al. 2006).

In some objects, observations show that the redshifted absorption component is rather persistently present in higher Balmer lines, e.g. in $\text{H}\gamma$ and $\text{H}\delta$ in DR Tau and YY Ori (e.g. Aiad et al. 1984; Appenzeller et al. 1988; Edwards et al. 1994), in $\text{H}\delta$ in DF Tau and RW Aur A (e.g. Edwards et al. 1994). This contradicts with our stable accretion model (Fig. 3) in which gas flows on to the star occurs in two ordered funnel streams, and a redshifted absorption is present only during a part of the whole rotational phase – when the funnel stream on the upper hemisphere is located in the line of sight of an observer to the stellar surface. However, a persistent redshifted absorption could be observed also in a stable accretion model when the system is viewed pole-on because the hot spot and the accretion funnel stream on one hemisphere is visible for an observer during a complete rotational phase (e.g. see Figure 5 in Kurosawa et al. 2008).

No clear periodicity in the line variability is found in many CTTs. For example, in the observation of TW Hya, Donati et al. (2011b) found that the variability of $\text{H}\alpha$ and $\text{H}\beta$ are not periodic (but see also Alencar & Batalha 2002), and suggested the cause of the variability is intrinsic (e.g. changes in the mass-accretion rates) rather than the stellar rotation. TW Hya also shows the redshifted absorption component in near infrared hydrogen lines ($\text{Pa}\beta$, $\text{Pa}\gamma$ and $\text{Br}\gamma$) in multiple occasions (e.g. Edwards et al. 2006; Vacca & Sandell 2011); however, the frequency of the occurrence is unclear. In the studies of DR Tau by Alencar, Johns-Krull & Basri (2001) and DF Tau by Johns-Krull & Basri (1997), no clear periodicity was found in their line variability observations. The non-periodic behaviour of the line variability is consistent with our unstable accretion model (Figs. 4 and 5). On the other hand, clear signs of periodicity are found in the line variability in some of CTTs, e.g. BP Tau (e.g. Gullbring et al. 1996; Donati et al. 2008) and V2129 Oph (e.g. Donati et al. 2007; Donati et al. 2011a; Alencar et al. 2012). In the line variability study of V2129 Oph, Alencar et al. (2012) found that the redshifted absorption component in $\text{H}\beta$ was visible only during certain rotational phases. This is consistent with our stable accretion model (Fig. 3).

4.2 Photometric Variability

Observations show a variety of photometric variability in CTTs (e.g. Bouvier et al. 1993; Gahm et al. 1993; Herbst et al. 1994; Bouvier et al. 1995, 2003; Stassun et al. 1999; Herbst, Maley & Williams 2000; Oudmajer et al. 2001; Lamm et al. 2004; Alencar et al. 2010). In some stars, clear periodic light-curves are observed, while in others, the light curves appear stochastic (e.g., Herbst et al. 1994; Alencar et al. 2010). Although the variability in X-ray are mostly stochastic, in some cases, signs of rotational modulation are found in soft X-ray emission in CTTs (e.g.

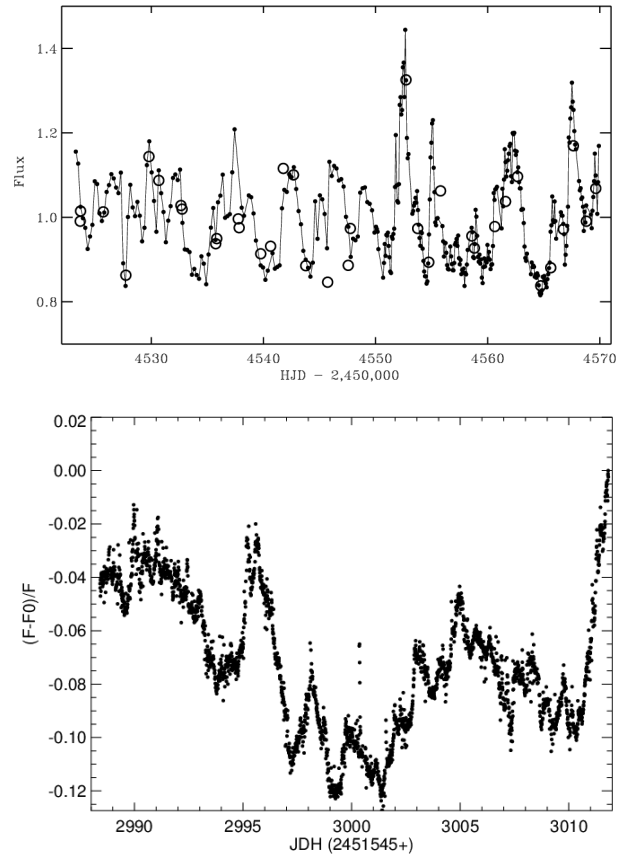


Figure 6. Top panel: the light-curve of TW Hya with the new broadband (located between V and R band) filter on *MOST* satellite (filled circle) overplotted with the V -band observation (open circle) of All Sky Automated Survey (from Figure 4 in Rucinski et al. 2008). Bottom panel: A typical stochastic light-curve (in ‘white light’ broadband) obtained by *CoRoT* satellite (from panel e of Fig. 1 in Alencar et al. 2010). Here, F and F_0 denote the flux and the maximum flux in the light curve, respectively. Credit: (upper panel) Rucinski et al. (2008), reproduced with permissions; (lower panel) Alencar et al. (2010), reproduced with permission © ESO.

Flaccomio et al. 2005; Flaccomio, Micela & Sciortino 2012). The well-ordered and periodic light curves are likely connected with rotation of hot spots resulting from ordered magnetospheric accretion streams (e.g., Herbst et al. 1994), or from cold spots which represent regions of strong magnetic field. The exact origin of the stochastic variability is not well known, and there may be different causes. It was earlier suggested that stars with ordered light-curves are accreting in a stable regime while stars with stochastic light curves are in the unstable regime (e.g., Romanova et al. 2008; Kulkarni & Romanova 2008, 2009).

Examples of periodic light curves can be found in e.g. Herbst et al. (1994) and Alencar et al. (2010). Using the CONvection ROTation and planetary Transits (*CoRoT*) satellite, Alencar et al. (2010) have shown that about 34 per cent of CTTs in the young stellar cluster NGC 2264 display clearly periodic light curves with one or two maxima per stellar rotation (see panels a and b in their Fig. 1). Our model light curve from the stable accretion regime (Fig. 5) is very similar to the periodic light curves with two maxima per rotation. As in the observation, the smaller and larger maxima alternately appear. The periodic light curves with one maximum are also

consistent with a stable accretion observed with a lower inclination angle system (e.g. Figure 4 in Kurosawa et al. 2008).

Examples of irregular light curves are shown in Fig. 6. The figure shows the light curve of TW Hya obtained with the Microvariability & Oscillations of STars (*MOST*) satellite presented in Rucinski et al. (2008) and the *CoRoT* light curve of a CTTS in NGC 2264 presented in Alencar et al. (2010). Irregular light curves are found in about 39 per cent of the CTTSs sample in Alencar et al. (2010). Rucinski et al. (2008) finds no clear periodicity in the light curve for TW Hya in Fig. 6. However, they determined an approximate period of 3.7 d based on the light curve in an earlier epoch which showed some periodic behaviour.⁴ Using the 3.7 d period, one can see that there are a few to several maxima per rotation in the light curve for TW Hya in Fig. 6. Interestingly, our model light curve for the unstable accretion regime (Fig. 5) also shows a few to several maxima per rotation. Similarly no clear period is found in the light curve of Alencar et al. (2010) in Fig. 6; however, the pattern of the variability resembles that of our model from the unstable accretion regime (Fig. 5). Further, the variability amplitudes of the irregular light curves in Fig. 6 are also comparable to the model in the unstable regime (Figs. 5 and A3).

In summary, we confirm that the periodic light curves found in the observations are consistent with a scenario in which the continuum variability are caused by the rotation of two hot spots which are naturally formed in a stable accretion regime with a tilted dipole magnetosphere. Although not included in our model, the presence of stable cold spots on a stellar surface would also produce a periodic light curve. On the other hand, the irregular light curves found in observations are consistent with a scenario in which the continuum variability are caused by the rotation of stochastically forming hot spots which naturally occurs in the unstable regime. Yet the third type of the light curve (AA Tau-like), in which the variability is partially caused by the occultation of a stellar surface by an accretion ‘disc wall’ or a warp near the disc truncation radius (e.g. Bouvier et al. 1999; Bertout 2000; Bouvier et al. 2007; Alencar et al. 2010; Romanova et al. 2013), is not considered in this paper.

5 DEPENDENCY ON MODEL PARAMETERS

In general, the light curves and line EW variability behaviours are expected to be similar among the MHD models which clearly show stable and ordered accretion flows. The stable accretion funnels will always form smooth and periodic light curves and line variability. On the other hand, light curves and line variability behaviour for the unstable regimes will be slightly different, depending on the strength of the instability. In earlier models, (e.g. Kulkarni & Romanova 2008; Kulkarni & Romanova 2009), we have found that the number of unstable accretion filaments or ‘tongues’ present at a given moment of time decreases from several to just one or two as the instability changes from a strong regime to a weak regime. While the number of tongues may change for different model parameters, the occurrences of the unstable tongues are still non-periodic. Therefore, the corresponding light curves and line variability will also remain non-periodic, similar to those seen in the unstable model in this paper (Fig. 5). However, the frequency of the peaks in the light curves and line EW curves per stellar rotation will decrease when the instability becomes weaker. Such variations

are expected during the transition from a strongly unstable regime to a stable regime. The strength of the instability depends on some MHD model parameters such as P_* , r_{cor} , Θ and α in Table 1. In the following we briefly discuss the dependency of our model on these key model parameters that can influence the stability of the accretion flows.

Dependency on P_ and r_{cor} .* These are essentially the same model parameters since the corotation radius (r_{cor}) is determined by the stellar rotation period P_* for a given stellar mass (M_*), i.e. $r_{\text{cor}} = (GM_*)^{1/3}(P_*/2\pi)^{2/3}$. The unstable flows occur more easily when the effective gravity (including the effect of the centrifugal force) is stronger at the inner rim of the accretion disc (e.g. Spruit et al. 1995). A slower stellar rotation or equivalently a larger r_{cor} will increase the effective gravity; hence, it tends to enhance the instability. The effective gravity becomes negative at the disc-magnetosphere boundary when r_{cor} becomes larger than the truncation (magnetospheric) radius r_m (where the matter stress in the disc becomes comparable with the magnetic stress in the magnetosphere). Hence, in this simplified approach, accretion flows are expected to become unstable when $r_m < r_{\text{cor}}$ (e.g. Spruit & Taam 1993). However, the onset of instability depends on a few other factors, such as the level of differential rotation in the inner disc, and also on the gradient of the ratio between the disc surface density and magnetic flux (e.g. Kaisig, Tajima & Lovelace 1992; Lubow & Spruit 1995; Spruit et al. 1995). Hence, the condition, $r_m < r_{\text{cor}}$, is necessary for the onset of instability, but it may not be sufficient. In general, we find the instability is strong in our MHD simulations when stars are rotating relatively slowly i.e. $r_m < r_{\text{cor}}$. Consequently, we have chosen a larger P_* for the unstable case and a smaller P_* for the stable case in this paper.

Dependency on Θ . The instability can occur at different misalignment angles of the dipole Θ . However, at a large Θ (when the dipole is strongly tilted), the accretion flow becomes more stable because the magnetic poles are closer to the inner rim of the disc. The potential barrier in the vertical direction that the gas at the inner rim of the disc has to overcome to form the stable funnel accretion flow is reduced at a high Θ angle (Kulkarni & Romanova 2009). On the other hand, when Θ becomes small, the potential barrier to overcome becomes higher, and the stable accretion funnels cannot be formed so easily. In this case, the gas accumulates at the inner rim of the disc, and the accretion on to the star proceeds through instability ‘tongues’ which penetrate through the magnetosphere. In our MHD simulations, we find that a strong instability occurs when $\Theta < 25^\circ$ (Kulkarni & Romanova 2009). Therefore, in this paper, we have chosen the large tilt angle $\Theta = 30^\circ$ to demonstrate the accretion in the stable case, and the small tilt angle $\Theta = 5^\circ$ in the unstable case.

Dependency on α . We use the viscosity parameter (α) to control the global mass-accretion rate. The initial density conditions for the disc are common in all of our models, including the ones presented in the past (e.g. Kulkarni & Romanova 2008). The higher the value of α , the higher the mass-accretion rate becomes. At a higher accretion rate, the inner edge of the disc moves closer to the star. Consequently the ratio r_m/r_{cor} becomes smaller, and the condition becomes more favourable for the instability. The compression of gas near the magnetosphere (the enhanced surface density per unit magnetic flux) may also play a role. The possible artifacts of the α viscosity on the formation of instability have been studied in a few experiments. For example, we start from a stable case with a small viscosity ($\alpha = 0.02$), which is used for the stable case as in Table 1, and we increase the initial density in the disc by a factor of 2. In this case, we have observed that the accretion becomes unsta-

⁴ This may be a quasi-period or drifting period (see also Siwak et al. 2011).

ble (Romanova et al. 2008). In another experiment, we start from a relatively small viscosity ($\alpha = 0.04$), and increase the period of the star P_* . In this case, we find the accretion becomes strongly unstable (e.g. see Fig. 10 in Kulkarni & Romanova 2009). Moreover, in our recent simulations with the grid resolutions twice of those in the simulations presented in this paper (i.e. $N_r \times N^2 = 160 \times 61^2$) but with a smaller viscosity ($\alpha = 0.02$), we find the accretions flow also become unstable, if a star rotates relatively slowly (e.g. see Fig. 17 in Romanova et al. 2013). Based on these experiments, we conclude that a large α is not a necessary condition for the instability. For the MHD simulations presented in this paper, we have used $\alpha = 0.1$ in the unstable case and $\alpha = 0.02$ in the stable case for the consistency with earlier simulations (e.g. Romanova et al. 2008; Kulkarni & Romanova 2009).

6 CONCLUSIONS

We have investigated observational properties of CTTs accreting in the stable and unstable regimes using (a) 3D MHD simulations to model matter flows, and (b) 3D radiative transfer models to calculate time-series hydrogen line profiles and continuum emissions. In modelling line profiles, we have introduced the parameterized temperature structures of Hartmann et al. (1994) in the accretion flow (Section 2.2) and a fixed hot spot temperature (Section 3.2) in order to match the predicted line strengths and the amplitudes of light curves more closely to observations. Our approach is to introduce minimal modifications to the MHD solutions to obtain reasonable line profiles and light curves. Although this is not completely consistent with the MHD solutions, we still retain the flow geometry, density and velocity information from the MHD simulations. To implement proper heating/cooling mechanisms in the flows and more realistic hot spots, we need to develop proper physical models for them, which we have not done yet.

In this work, we have focused on the variability in the time scale comparable with or less than a rotational period. For the unstable accretion model, we have considered the flows associated with the Rayleigh-Taylor instability that occurs at the interfaces between the accretion disc and stellar magnetosphere. In particular, we have analyzed qualitative behaviours of the variability in the redshifted absorption component in $H\delta$ and the continuum flux to find key observational signatures that can distinguish CTTs accreting in the two different regimes (stable and unstable). Our main findings are summarized in the following:

(1) In the stable regime, the emission lines vary smoothly (Fig. 3), and their line EW show one or two peaks per stellar rotation period (Fig. 5). In the unstable regime, the EW of spectral lines vary irregularly and more frequently — showing several maxima per stellar rotation period (Fig. 5).

(2) In the stable regime, the redshifted absorption is observed during approximately one half of the rotation period (when one of two accretion streams is located in front of an observer), and is absent during another half of the period (Fig. 3). In the unstable regime, the redshifted absorption is observed at most of the rotational phases due to the presence of several unstable tongues/accretion streams which frequently move into the line of sight of an observer to the stellar surface (Fig. 4).

(3) In the stable regime, the continuum emission from hot spots (the light-curve) varies smoothly, and it has two peaks per stellar rotation period (Fig. 5). In the unstable regime, the light-curve shows irregular variability with several peaks per period corresponding to several unstable tongues (Fig. 5).

We find that the redshifted absorption components are in general more visible in the higher Balmer series, e.g. in $H\delta$ and $H\gamma$ (see Figs. A1 and A2) and some near-infrared hydrogen lines such as $Pa\beta$ and $Br\gamma$ than in the lower Balmer lines ($H\alpha$ and $H\beta$). Although the line variability analysis presented here is mainly based on $H\delta$, similar conclusions can be reached if we use the other redshifted absorption sensitive lines mentioned above. In addition to these hydrogen lines, He I $\lambda 10830$ may be also useful for probing the accretion stream geometry of CTTs, as demonstrated by Fischer et al. (2008).

The work presented here may help to differentiate possible mechanisms of variability. Since the irregular light curves found in many CTTs can be connected with different physical processes (e.g. magnetic flares, an accretion from a turbulent disc, an accretion through an instability), the additional information from a line profile variability analysis may help to disentangle the different processes. For example, magnetic flares are not relevant to an accretion process; hence, no correlation is expected between a light curve and a redshifted absorption (which characterizes the magnetospheric flows). If a light curve is irregular and the redshifted absorption is persistent and non-periodic, the system may be accreting through an instability, which can occur either from a laminar, or from a turbulent disc. On the other hand, if a light curve is irregular and the redshifted absorption is periodic (seen only during a part of a rotational phase), the system may be accreting through well-defined accretion funnels originating from a turbulent disc, which provides turbulent cells to the accretion funnels and consequently produces an irregular light curve.

We have investigated only the case of a strong instability in which most of the matter accretes in the unstable equatorial tongues. However, in reality, many CTTs may be in a moderately unstable accretion regime (e.g. Kulkarni & Romanova 2009) in which both ordered funnel flows and chaotic tongues are present. In these cases, both a persistent redshifted absorption component associated with the unstable accretion tongues, and ordered variability pattern associated with the stable accretion streams can be present simultaneously. However, if the two ordered accretion streams from the stable flow components dominate, one can expect only one redshifted absorption per stellar rotation period as seen in the current work (e.g. Fig. 3). Interestingly, a recent study by Romanova & Kulkarni (2009) has shown that the unstable flows can be more ordered and corotate with the inner disc when the size of magnetosphere is small and comparable with the radius of the star. They have also shown that the formation of unstable tongues can be driven by the density waves formed in the inner disc region and by the interaction of the inner disc with the tilted magnetic dipole field of the star (Romanova et al. 2012).

Although we have concentrated on the line variability associated with the magnetospheric accretion, some line variability could be also attributed to a variable nature of the wind. The winds from the disc-magnetosphere boundary (e.g. Shu et al. 1994) are usually associated with episodic inflations and openings of the field lines connecting the magnetosphere and the disc on a time-scale of a few inner disc rotations (Aly & Kijpers 1990; Goodson et al. 1997; Romanova et al. 2009; Zanni & Ferreira 2012). If the line emission from a wind (either stellar or disc) is not significant, a variable wind would cause a variability mainly in the blueshifted absorption component. However, the emission from the wind could contribute non-negligibly to a total line emission (e.g. Kurosawa et al. 2006; Lima et al. 2010; Kwan & Fischer 2011; Kurosawa & Romanova 2012). If this is so, it makes the interpretation of a line variability a harder problem. On the other hand, some near-infrared hydrogen

lines e.g. Pa β and Br γ , which show relatively strong redshifted absorption in our models (Fig A2), are usually not affected by the winds (e.g. Folha & Emerson 2001); therefore, the diagnostic tools presented in this paper are still valid. In addition, the main time-scale of variability associated with winds is expected to be longer than that of the magnetospheric accretion considered in this paper.

ACKNOWLEDGMENTS

We thank an anonymous referee who provided us valuable comments and suggestions which helped improving the manuscript. We thank S. H. P. Alencar and S. M. Rucinski for allowing us to use their figures in this work. RK thanks Vladimir Grinin for a helpful discussion and P. P. Petrov for an example of a variable CTTS. RK also thanks Tim Harries, the original code author of TORUS, for his support. Resources supporting this work were provided by the NASA High-End Computing (HEC) Program through the NASA Advanced Supercomputing (NAS) Division at Ames Research Center and the NASA Center for Computational Sciences (NCCS) at Goddard Space Flight Center. The research was supported by NASA grants NNX10AF63G, NNX11AF33G and NSF grant AST-1008636.

REFERENCES

- Aiad A., Appenzeller I., Bertout C., Stahl O., Wolf B., Isobe S., Shimizu M., Walker M. F., 1984, *A&A*, 130, 67
- Alencar S. H. P., Johns-Krull C. M., Basri G., 2001, *AJ*, 122, 3335
- Alencar S. H. P., Batalha C., 2002, *ApJ*, 571, 378
- Alencar S. H. P., Basri G., Hartmann L., Calvet N., 2005, *A&A*, 440, 595
- Alencar, S. H. P. et al., 2010, *A&A*, 519, A88
- Alencar S. H. P. et al., 2012, *A&A*, 541, 116
- Aly J. J., Kuijpers J., *A&A*, 227, 473
- Appenzeller I., Jetter R., Jankovics I., 1986, *A&AS*, 64, 65
- Appenzeller I., Reitermann A., Stahl O., 1988, *PASP*, 100, 815
- Arons J., Lea S. M., 1976, *ApJ*, 207, 914
- Bachetti M., Romanova M. M., Kulkarni A. K., Burderi L., di Salvo T., 2010, *MNRAS*, 403, 1193
- Beristain G., Edwards S., Kwan J., 2001, *ApJ*, 551, 1037
- Bertout C., 2000, *A&A*, 363, 984
- Bouvier J., Cabrit S., Fernandez M., Martin E. L., Matthews, J. M., 1993, *A&A*, 272, 176
- Bouvier J., Covino E., Kovo O., Martin E. L., Matthews J. M., Terranegra L., Beck S. C., 1995, *A&A*, 299, 89
- Bouvier J. et al., 1999, *A&A*, 349, 619
- Bouvier J. et al., 2003, *A&A*, 409, 169
- Bouvier J. et al., 2007, *A&A*, 463, 1017
- Camenzind M., 1990, *Reviews in Modern Astronomy*, 3, 234
- Castor J. I., 1970, *MNRAS*, 149, 11
- Calvet N., Gullbring E. 1998, *ApJ*, 509, 802
- Chelli A., Cruz-Gonzalez I., Salas L., Ruiz E., Carrasco L., Reillas E., 1997, in Malbet F., Castet A., eds., *Poster Proc. IAU Symp 182. Low Mass Star Formation – from Infall to Outflow. Laboratoire d’Astrophysique, Grenoble*, p. 263
- Costigan G., Scholz A., Stelzer B., Ray T., Vink J. S., Mohanty S., 2012, *MNRAS*, 427, 1344
- Donati J.-F. et al., 2007, *MNRAS*, 380, 1297
- Donati J.-F. et al., 2008, *MNRAS*, 386, 1234
- Donati J.-F. et al., 2010, *MNRAS*, 409, 1347
- Donati J.-F. et al., 2011a, *MNRAS*, 412, 2454
- Donati J.-F. et al., 2011b, *MNRAS*, 417, 472
- Edwards S., 1979, *PASP*, 91, 329
- Edwards S., Hartigan P., Ghandour L., Andrusis, C., 1994, *AJ*, 108, 1056
- Edwards S., Fischer W., Hillenbrand L., Kwan J., 2006, *ApJ*, 646, 319
- Faesi C. M. et al., 2012, *PASP*, 124, 1137
- Feigelson E., Townsley L., Güdel M., Stassun K., 2007, in Reipurth B., Jewitt D., Keil K., eds, *Protostars and Planets V*. Univ. Arizona Press, Tucson, p 313
- Fischer W., Kwan J., Edwards S., Hillenbrand L., 2008, *ApJ*, 687, 1117
- Flaccomio E., Micela G., Sciortino S., Feigelson E. D., Herbst W., Favata F., Harnden F. R., Jr., Vrtilik S. D., 2005, *ApJS*, 160, 450
- Flaccomio E., Micela G., Sciortino S., 2012, *A&A*, 548, 85
- Folha D. F. M., Emerson J. P., 2001, *A&A*, 365, 90
- Gahm G. F., Gullbring E., Fischerstrom C., Lindroos K. P., Loden K., 1993, *A&AS*, 100, 371
- Goodson A. P., Winglee R. M., Boehm, K.-H., 1997, *ApJ*, 489, 199
- Gullbring E., Petrov P. P., Ilyin I., Tuominen I., Gahm G. F., Loden K., 1996, *A&A*, 314, 835
- Gullbring E., Calvet N., Muzerolle J., Hartmann L., 2000, *ApJ*, 544, 927
- Harries T. J., 2000, *MNRAS*, 315, 722
- Harries T. J., 2011, *MNRAS*, 416, 1500
- Hartmann L., Avrett E., Edwards S., 1982, *ApJ*, 261, 279
- Hartmann L., Hewett R., Calvet N., 1994, 426, 669
- Herbst W., Maley J. A., Williams E. C., 2000, *AJ*, 120, 349
- Herbst W., Herbst D. K., Grossman E. J., Weinstein D., 1994, *AJ*, 108, 1906
- Herbst W., Bailer-Jones C. A. L., Mundt R., Meisenheimer K., Wackermann R., 2002, *A&A*, 396, 513
- Hawley J.F., 2000, *ApJ*, 528, 462
- Johns C. M., Basri G., 1995a, *AJ*, 109, 2800
- Johns C. M., Basri G., 1995b, *ApJ*, 449, 341
- Johns-Krull C. M., Basri G., 1997, *ApJ*, 474, 433
- Kaisig M., Tajima T., Lovelace R. V. E., 1992, *ApJ*, 386, 83
- Klein R. I., Castor J. I., 1978, *ApJ*, 220, 902
- Königl A., 1991, *ApJ*, 370, L39
- Koldoba A. V., Romanova M. M., Ustyugova G. V., Lovelace R. V. E., 2002, *ApJ*, 576, L53
- Koldoba A. V., Romanova M. M., Ustyugova G. V., Lovelace R. V. E., 2008, *MNRAS*, 388, 357
- Krautter J., Appenzeller I., Jankovics I., 1990, *A&A*, 236, 416
- Kulkarni, A., Romanova M. M., 2005, *ApJ*, 633, 349
- Kulkarni, A., & Romanova, M.M. 2008, *ApJ*, 386, 673
- Kulkarni, A., & Romanova, M.M. 2009, *ApJ*, 398, 701
- Kurosawa R., Harries T. J., Bate M. R., Symington N. H., 2004, *MNRAS*, 351, 1134
- Kurosawa R., Harries T. J., Symington N. H., 2005, *MNRAS*, 358, 671
- Kurosawa R., Harries T. J., Symington N. H., 2006, *MNRAS*, 370, 580
- Kurosawa R., Romanova M. M., Harries T. J., 2008, *MNRAS*, 385, 1931
- Kurosawa R., Romanova M. M., Harries T. J., 2011, *MNRAS*, 416, 2623
- Kurosawa R., Romanova M. M., 2012, *MNRAS*, 426, 2901
- Kwan J., Fischer W., 2011, *MNRAS*, 411, 2383
- Kurucz R. L., 1979, *ApJS*, 40, 1

- Lamm M. H., Bailer-Jones C. A. L., Mundt R., Herbst W., Scholz A., 2004, *A&A*, 417, 557
- Li L.-X., Narayan R., 2004, *ApJ*, 601, 414
- Lima G. H. R. A., Alencar S. H. P., Calvet N., Hartmann L., Muzerolle J., 2010, *A&A*, 522, A104
- Long M., Romanova M. M., Lovelace R. V. E., 2007, *MNRAS*, 374, 436
- Long M., Romanova M. M., Lovelace R. V. E., 2008, *MNRAS*, 386, 1274
- Long M., Romanova M. M., Lamb F., Kulkarni A. K., Donati J.-F., 2011, *MNRAS*, 413, 1061
- Lovelace R. V. E., Romanova M. M., Bisnovatyi-Kogan G.S., 1995, *MNRAS*, 275, 244
- Lubow S. H., Spruit H. C., 1995, *ApJ*, 445, 337
- Muzerolle J., Calvet N., Hartmann L., 1998, *ApJ*, 492, 743
- Muzerolle J., Calvet N., Hartmann L., 2001, *ApJ*, 550, 944
- Oliveira J. M., Foing B. H., van Loon J. T., Unruh Y. C., 2000, *A&A*, 362, 615
- Oudmaijer R. D. et al., 2001, *A&A*, 379, 564
- Petrov P. P., Gullbring E., Ilyin I., Gahm G. F., Tuominen I., Hackman T., Loden K., 1996, *A&A*, 314, 821
- Petrov P. P., Zajtseva G. V., Efimov Y. S., Duemmler R., Ilyin I. V., Tuominen I., Shcherbakov V. A., 1999, *A&A*, 341, 553
- Petrov P. P., Gahm G. F., Gameiro J. F., Duemmler R., Ilyin I. V., Laakkonen T., Lago M. T. V. T., Tuominen I., 2001, *A&A*, 369, 993
- Reipurth B., Pedrosa A., Lago M. T. V. T., 1996, *A&AS*, 120, 229
- Romanova M. M., Ustyugova G. V., Koldoba A. V., Lovelace R. V. E., 2002, *ApJ*, 578, 420
- Romanova M. M., Ustyugova G. V., Koldoba A. V., Lovelace R. V. E., 2003, *ApJ*, 595, 1009
- Romanova M. M., Ustyugova G. V., Koldoba A. V., Lovelace R. V. E., 2004, *ApJ*, 610, 920 (ROM04)
- Romanova M. M., Kulkarni A. K., Lovelace R. V. E., 2008, *ApJ*, 273, L171
- Romanova M. M., Kulkarni, A. K., 2009, *MNRAS*, 398, 1105
- Romanova M. M., Ustyugova G. V., Koldoba A. V., Lovelace R. V. E., 2009, *MNRAS*, 399, 1802
- Romanova M. M., Long M., Lamb F., Kulkarni A. K., Donati J.-F., 2011, *MNRAS*, 411, 915
- Romanova M. M., Ustyugova G. V., Koldoba A. V., Lovelace R. V. E., 2012, *MNRAS*, 421, 63
- Romanova M.M., Ustyugova G. V., Koldoba A. V., Lovelace R. V. E., 2013, *MNRAS*, in press (astro-ph/1209.1161)
- Rucinski S. M. et al., 2008, *MNRAS*, 391, 1913
- Rybicki G. B., Hummer D. G., 1978, *ApJ*, 219, 654
- Powell K. G., Roe P. L., Linde T. J., Gombosi T. I., De Zeeuw D. L. 1999, *J. Comp. Phys.*, 154, 284
- Sacco G. G., Orlando S., Argiroffi C., Maggio A., Peres G., Reale F., Curran R. L., 2010, *A&A*, 522, 55
- Shakura N. I., Sunyaev R. A., 1973, *A&A*, 24, 337
- Shu F., Najita J., Ostriker E., Wilkin F., Ruden S., Lizano S., 1994, *ApJ*, 429, 781
- Siwak M. et al., 2011, *MNRAS*, 410, 2725
- Smith K. W., Lewis G. F., Bonnell I. A., Bunclark P. S., Emerson J. P., 1999, *MNRAS*, 304, 367
- Sobolev V. V., 1957, *Soviet Astronomy*, 1, 678
- Spruit H. C., Taam R. E., 1993, *A&A*, 402, 593
- Spruit H. C., Stehle R., & Papaloizou J. C. B., 1995, *MNRAS*, 275, 1223
- Stassun K. G., Mathieu R. D., Mazeh T., Vrba F. J., 1999, *AJ*, 117, 2941
- Stempels H. C., Piskunov N., 2002, *A&A*, 391, 595
- Stone J. M., Gammie C. F., Balbus S. A., Hawley J. F., 2000, in Mannings V., Boss A. P., Russell S. S., eds., *Protostars and Planets IV* Univ. Arizona Press, Tucson, p 589
- Symington N. H., Harries T. J., Kurosawa R., 2005, *MNRAS*, 356, 1489
- Tsang D., Lai D., 2009, *MNRAS*, 396, 589
- Ustyugova G. V., Koldoba A. V., Romanova M. M., Lovelace R. V. E., 2006, *ApJ*, 646, 304
- Vacca W. D., Sandell G., 2011, *ApJ*, 732, 8
- Valenti J. A., Basri G., Johns C. M., 1993, *AJ*, 106, 2024
- Valenti J. A., Johns-Krull C. M., 2004, *Ap&SS*, 292, 619
- Wolk S. J., Harnden F. R., Jr., Flaccomio E., Micela G., Favata F., Shang H., Feigelson E. D., 2005, *ApJS*, 160, 423
- Zanni C., & Ferreira, J., 2012, *A&A*, in press (arXiv:1211.4844)

APPENDIX A: ADDITIONAL LINE AND CONTINUUM VARIABILITY MODELS

In the main text of the paper, we have used the subsets of $H\delta$ model profiles and the continuum flux near $H\delta$ to demonstrate the key observable differences between accretion in the stable and unstable regimes. In this section, we present (1) the time-series profiles of additional hydrogen lines, i.e. $H\alpha$, $H\beta$, $H\gamma$, $Pa\beta$ and $Br\gamma$ in the rotational phase (ϕ) between 0 and 0.96 with the interval $\Delta\phi = 0.16$ (Figs. A1 and A2) and (2) the line EW variability curves for the same additional lines as in (1), but for three rotational phases (between $\phi = 0$ and 2.96) with the interval $\Delta\phi = 0.04$ (Fig. A3). The variability curves of the continuum flux (light curves) at each line frequency are also shown in the same figure.

In Fig. A1, $H\alpha$ line profiles for both stable and unstable regimes show relatively small variability. No redshifted absorption component is seen in both cases. This is mainly because $H\alpha$ line emission occurs in a wider region in the accretion stream, not just near the base of the accretion stream (near the stellar surface), and the strong emission in the line wings due to line broadening effects (e.g. the Stark broadening, Muzerolle et al. 2001). The model profiles for $H\beta$ and $H\gamma$ show a very weak redshifted absorption component (below the continuum level) in both stable and unstable regimes at some rotational phases. Since the absorption component in these lines are very weak, they are not suitable for studying the differences between the stable and unstable regimes. Although not shown here, the redshifted absorption in these lines becomes more visible if the accretion funnel gas temperature is decreased slightly.

The redshifted absorption components are much more prominent in $H\delta$ (in optical), $Pa\beta$ and $Br\gamma$ (in near-infrared) as one can see in Fig. A2, for both stable and unstable cases. For the stable accretion case, the redshifted absorption component is visible in these lines during about a half of a rotational phase (between $\phi \sim 0$ and ~ 0.5). These phases approximately coincide with the phases when the upper accretion funnel stream is in front of the star (see Fig. 3), i.e. when the upper accretion funnel is in the line of sight of the observer to the stellar surface. A weak double-peak feature visible in $Pa\beta$ and $Br\gamma$ in the latter half of the rotational phase ($\phi \sim 0.5$ and ~ 1.0) is mainly caused by the ‘lack of emission’ from the gas moving at zero project velocity toward an observer. This is due to the geometrical effect (two distinct accretion streams) and the fact that the emission in $Pa\beta$ and $Br\gamma$ occurs near the base of accretion stream where the flow velocity is large ($\sim 200 \text{ km s}^{-1}$). At some phases, the gas at the inner edge of the accretion disc could also intersect the line of sight between the observer and the system, and

causes a small amount of absorption near the line centre since the intervening gas in the inner most part of the accretion disc is just rotating with a Keplerian velocity; hence, its projected velocity toward the observer would be around zero. This can also contribute to the double peaked appearances of Pa β and Br γ . For the unstable case, the redshifted absorption component in H δ , Pa β and Br γ is present at almost all phases. This is due to the geometry of the accretion flows (see Fig. 4). The instability causes a few to several accretion streams to be present in the system at all times. Hence, at least one of the accretion streams or tongues is almost always in the line of sight of the observer to the stellar surface, and producing the redshifted absorption component.

Finally, in Fig. A3, we summarize the light curves (monochromatic) computed at the frequencies around H α , H β , H γ , Pa β and Br γ along with their line EWs as a function of rotational phase (for three rotational phases) for both stable and unstable cases. Note that the plots for H δ are not shown here because they have been already shown in Fig. 5 in the main text (Section 3.2). While the light curves are very periodic for the stable case, they are quite irregular/stochastic for the unstable case. In the stable case, the light curves clearly show two maxima per period (except for the case in Br γ). These are caused by the rotation of the two hot spots on the stellar surface created by the two accretion streams (see Figs. 3 and 5). The line EW variability curves are also influenced by the presence of hot spots since they contribute significantly to the total continuum flux. However, in the light curve of Br γ for the stable case, the relative amplitudes are rather small and it is more difficult to see the maxima. The smaller amplitudes are seen because the relative flux contribution of the hot spot (assumed 8000 K and ~ 2 per cent surface coverage) to the total continuum flux is much smaller at the wavelength of Br γ (2.165 μm). The accretion streams on to the stellar surface and the hot spots are formed rather stochastically in the unstable cases, resulting in the irregular light curves. See the main text in Section 3.2 for a further discussion on the light curves and the temporal variability in line EWs.

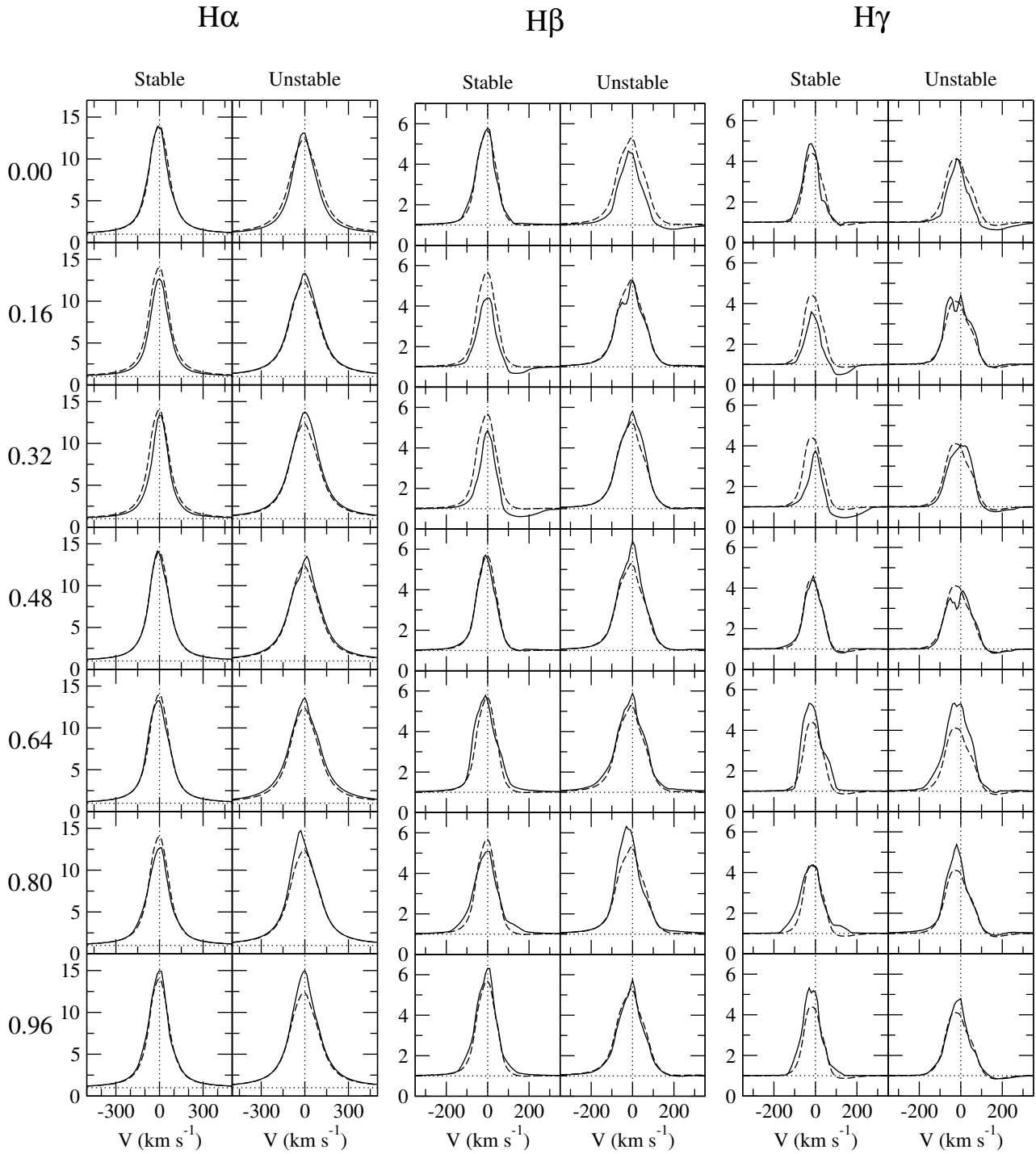


Figure A1. The time-series line profile models (solid) of H α , H β and H γ in the stable regime (left columns) and in the unstable regime (right columns) shown for different rotational phases (between 0 and 0.96). The rotational phase increases from the top to bottom panel, and the corresponding phase values are indicated in the leftmost column. In each panel, the line profile is compared with the mean profile (dashed, averaged over 3 rotational phases). All the profiles are computed with the system inclination angle $i = 60^\circ$.

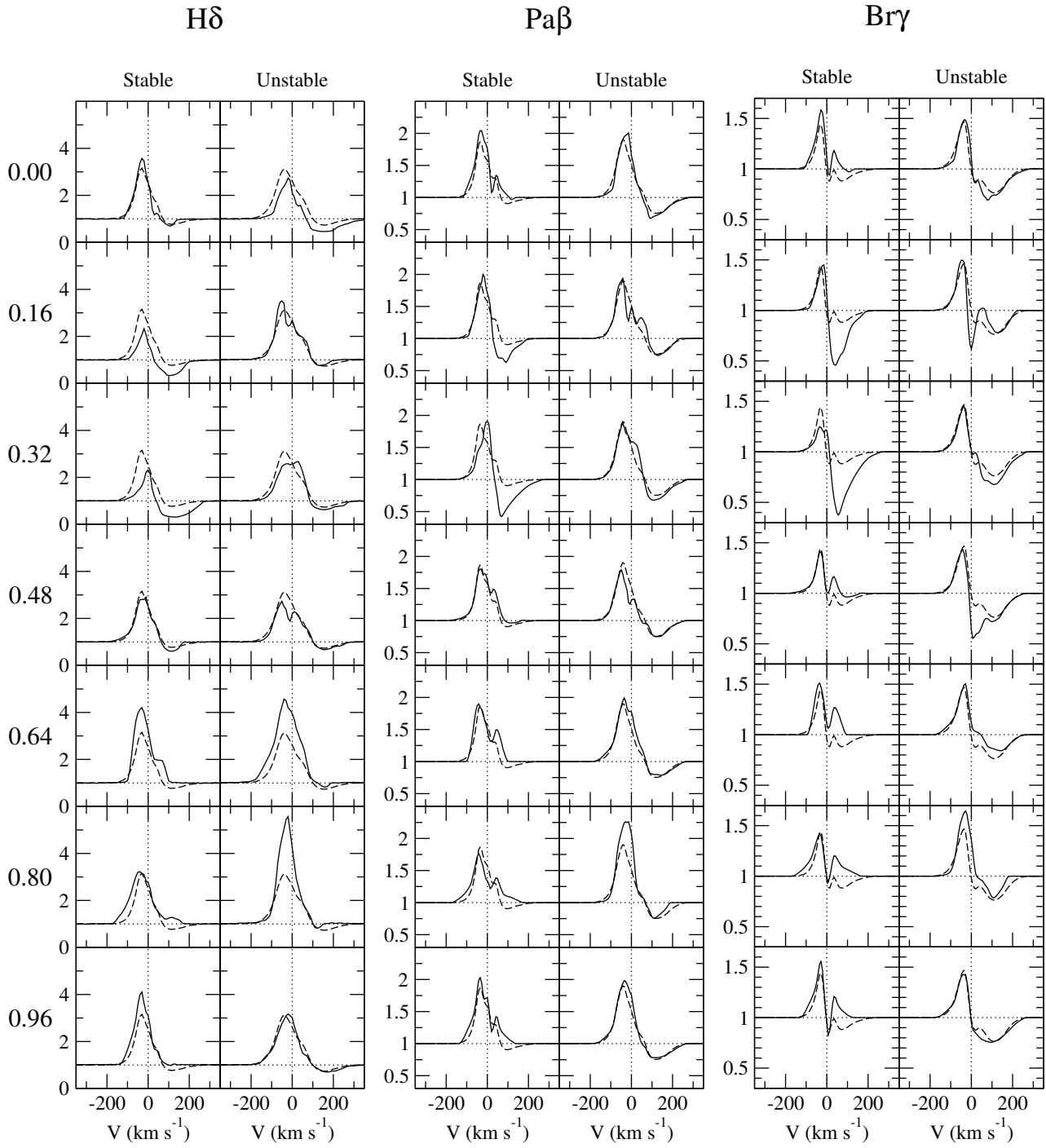


Figure A2. Same as in Fig. A1, but for $H\delta$, $Pa\beta$ and $Br\gamma$.

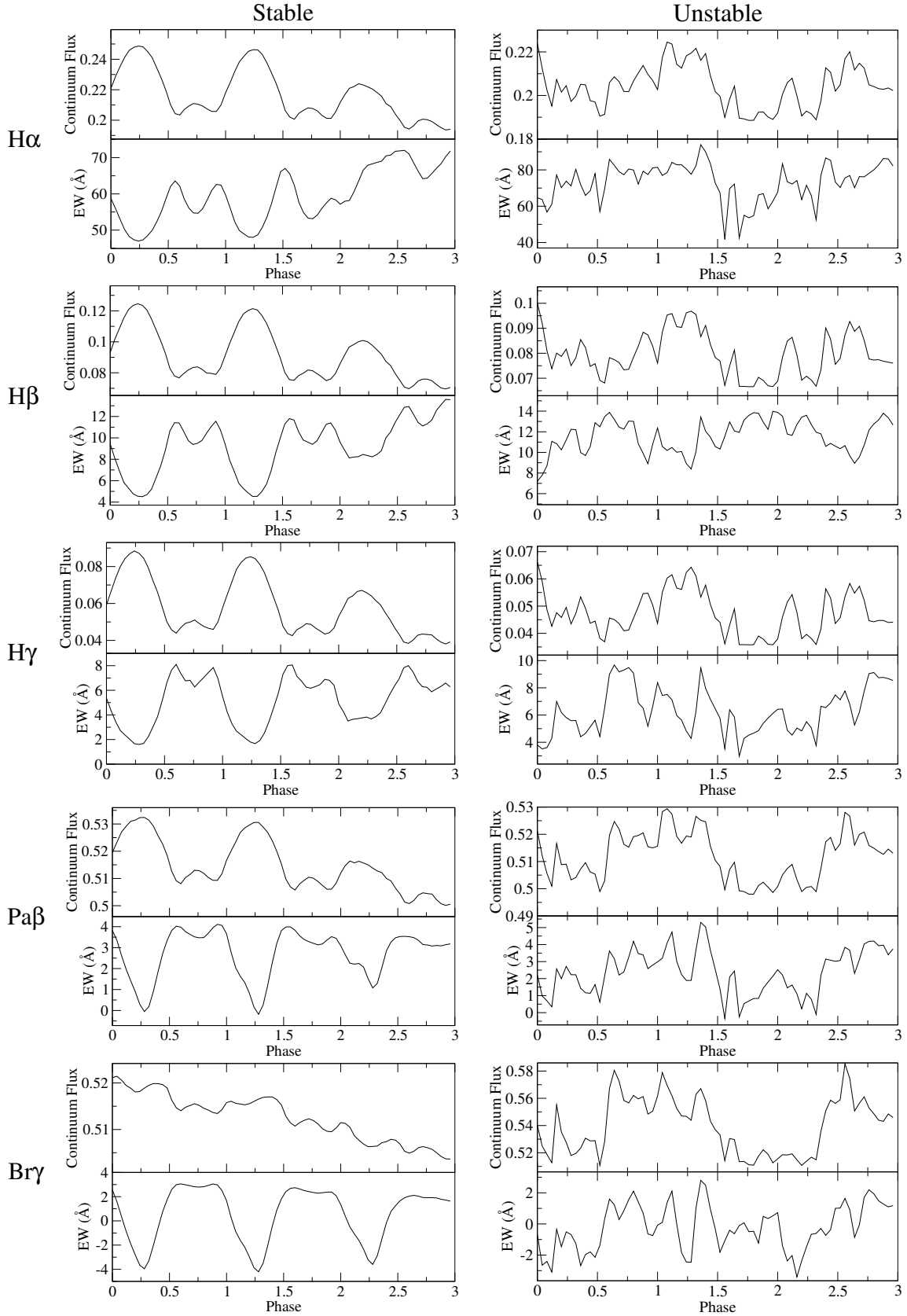


Figure A3. The temporal evolutions of the continuum flux (top panels, in arbitrary units) and the line equivalent width (bottom panels, in Å) of H α , H β , H γ , Pa β and Br γ in both stable (left columns) and unstable (right columns) regimes are shown for three rotational phases. The plots for H δ are omitted here since they have already been shown in Fig. 5 in the main text. The continuum fluxes are measured in the vicinity of the corresponding lines. In all cases, the system inclination angle $i = 60^\circ$ is used.

ONLINE SUPPORTING INFORMATION

APPENDIX B: ADDITIONAL FIGURES

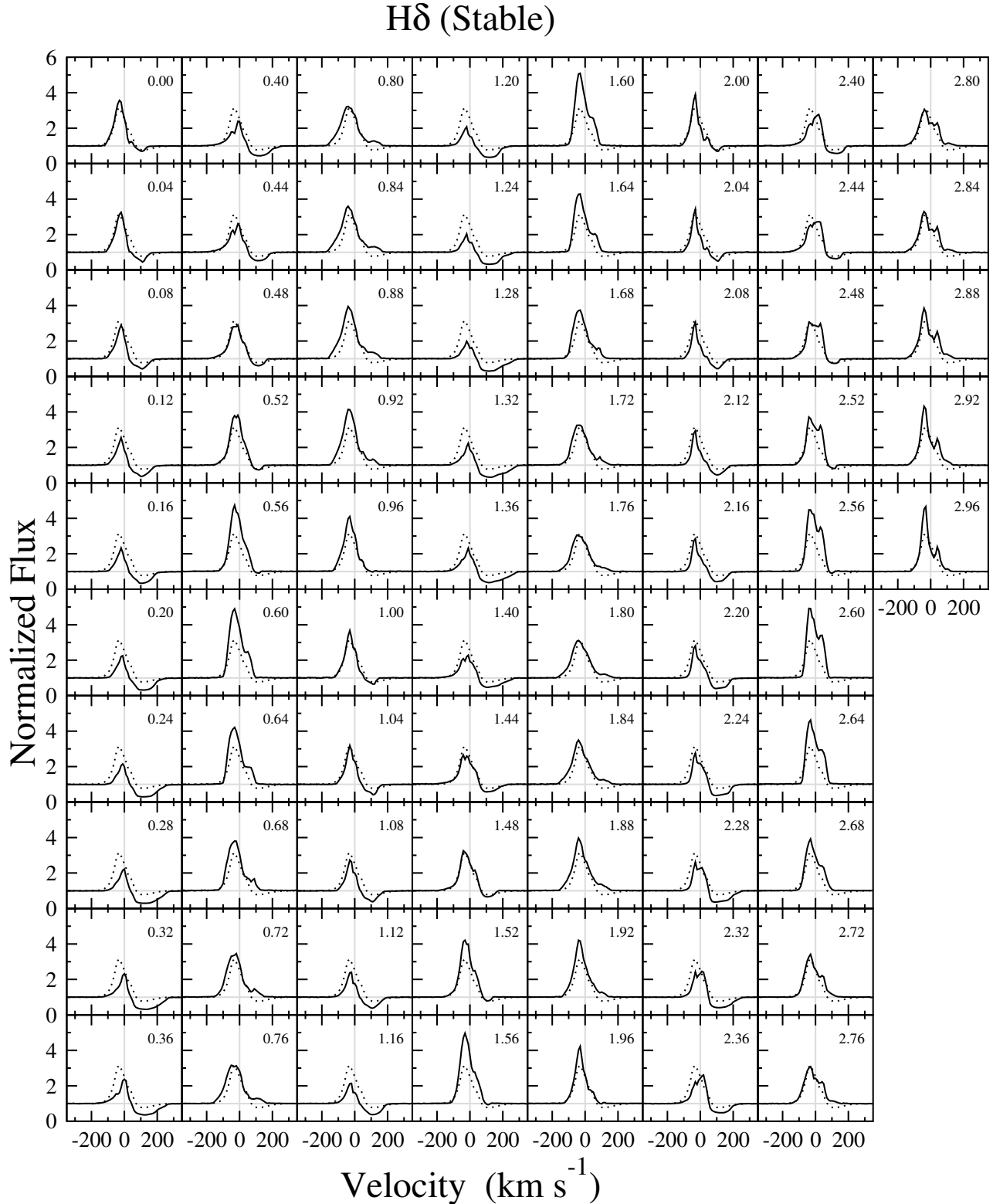


Figure B1. The temporal evolution of model $H\delta$ profiles (solid) for the stable accretion regime, computed for three rotation periods and with the system inclination angle $i = 60^\circ$. The profiles are computed every 0.04 of a whole phase. In total, 75 profiles are shown. The corresponding rotational phases are shown on the upper-right corners of each panel. The mean profile (dotted) from the 3 rotational phases is also shown in each panel, for a comparison.

H δ (Unstable)

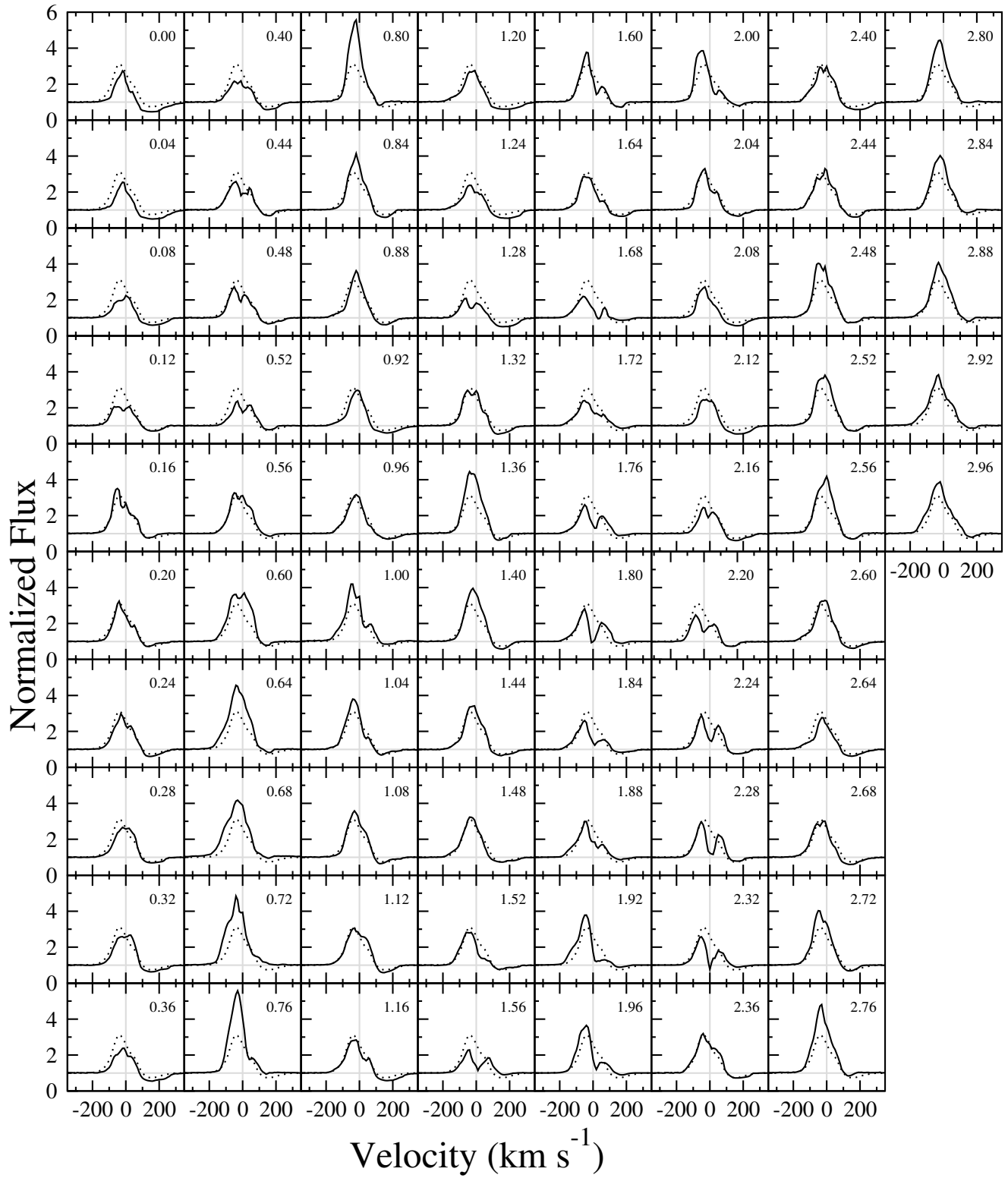


Figure B2. Same as in Fig. B1 but for the unstable regime.